Characterisation of 3D strain heterogeneity at the microstructure scale during Low Cycle Fatigue of an AlSi7Cu3Mg alloy at 250°C

Nathalie Limodin, Nora Dahdah, Long Wang, Ahmed El Bartali, Jean-François Witz, Jean-Yves Buffiere, Eric Charkaluk

Characterisation of 3D strain heterogeneity at the microstructure scale during Low Cycle Fatigue of an AlSi7Cu3Mg alloy at 250°C

Nathalie Limodin [a,1]*, Nora Dahdah[a], Long Wang[a2], Ahmed El Bartali[a], Jean-François Witz[a], Jean-Yves Buffiere[b], Eric Charkaluk[a3]

[a] Univ. Lille, CNRS, Centrale Lille, UMR 9013 - LaMcube - Laboratoire de Mécanique, Multiphysique, Multiéchelle, F-59000 Lille, France

[b] Laboratoire Matériaux, Ingénierie et Sciences (MATEIS), CNRS UMR5510, INSA-Lyon, 20 Av. Albert Einstein, 69621 Villeurbanne, France

Abstract

3D tomographic images of a cast AlSi7Cu3Mg alloy were obtained using synchrotron X-ray tomography during in-situ Low Cycle Fatigue tests at 250°C. While image analysis highlights the role of eutectic Si particles close to pores in damage mechanisms, high resolution digital volume correlation reveals the relationship between strain heterogeneity at the microstructural scale and hard particles failure or cracks. Monitoring strains evolution with cycles within hard particles, i.e. eutectic Si and Fe or Cu intermetallics, allows measuring their local failure strains and drawing a hierarchy of the deformation to failure. Then, a local Manson-Coffin curve per hard phase is proposed.

Keywords: Aluminium alloys, High temperature fatigue, Low cycle fatigue, Synchrotron radiation computed tomography, Digital volume correlation.

1 * Corresponding author. Email address: nathalie.limodin@centralelille.fr. Phone: +33 3 20 43 44 42

2 Present address: Science and Technology on Reliability and Environmental Engineering Laboratory, Beijing Institute of Structure and Environment Engineering, Beijing, China

3 Present address: Laboratoire de Mécanique des Solides - UMR 7649, Ecole Polytechnique, Palaiseau cedex, France

1 Introduction

Because of their high strength over weight ratio and good castability, thermal conductivity and corrosion resistance, aluminium-silicon (Al-Si) casting alloys are used in the car industry to manufacture structural components that must withstand thermomechanical fatigue (TMF) like engines. In recent years, Al-Si alloys, and the Lost Foam Casting (LFC) process were introduced to manufacture cylinder heads in a downsizing strategy. Indeed, while Al-Si alloys allow to reduce the weight, the near-net shape LFC process saves both material and cost compared to the conventional gravity Die Casting (DC) process [1]. However, the joint action of the pyrolysis gases [2] and low cooling rate (0.8°C/s) induces a larger number of pores and a coarser microstructure than the DC process [3]. This microstructure consists in pores and hard phases' particles, namely eutectic Si and copper (Cu) or iron (Fe) intermetallics, within an Al matrix. Strontium (Sr) is frequently added to modify the shape of eutectic Si from acicular to spheroidized or fibrous. However, the efficiency of this Sr-modification depends on the solidification cooling rate hence on the casting process. Understanding how this microstructure influences the in-service properties of the cylinder heads remains an open issue. The operating conditions on such components generate out-of-phase TMF [4]: the low-frequency temperature changes generate low-frequency variations of stresses/strains that can be assimilated to Low Cycle Fatigue (LCF) in compression at high temperature and in tension at Room Temperature (RT) with creation of cyclic plastic strain [5].

The state of the art on the LCF behaviour of Al-Si alloys is limited, especially at high temperature and the microstructure/property relationships differ according to the fatigue regime [6]. Table 1 summarizes the micromechanisms of fatigue damage in LCF at RT and high temperature reported in the literature.

At RT, several microstructural features affect the fatigue life of Al-Si alloys, e.g. Secondary Dendrite Arm Spacing (SDAS), pores, and hard phases' particles. A small SDAS (15-30µm) yields a longer crack initiation (75% of the total life) than a large SDAS (>50µm) for which crack initiation can stand for only 15% of the total life [7]. Because the SDAS increases as the solidification rate decreases, a large SDAS is interrelated with coarse hard particles and large pores whose detrimental role was evidenced in LCF [7–11]. Indeed, a high porosity content reduces the fatigue life [8] mostly due to the stringent role of the largest pores [7–11] on crack initiation (Table 1). When pores are below a critical size [12], LCF cracks

also initiate from hard particles [13][14], at eutectic Si [13,15,16] but also at Cu intermetallics [15]. Although Fe is a common impurity in secondary Al alloys that are obtained from recycling and remelting Al scraps, its influence in LCF is still controversial either on crack initiation, growth or total fatigue life (Table 1).

Table 1: Micromechanisms of LCF damage in AlSiCu alloys at RT and high temperature; grey cell highlights controversial results while empty cell highlights a lack of information.

<table>
<tr><th></th><th></th><th>Pores</th><th>Eutectic Si</th><th>Fe intermetallics</th><th>Cu intermetallics</th></tr>
<tr><td rowspan="5">Room temperature Low Cycle Fatigue (LCF)</td><td rowspan="2">Cracks initiate (N_i)</td><td rowspan="2">at the largest pores [7–11] at or close to the surface [8–10,12,17] and in subsurface [11]</td><td colspan="3">at hard particles when pores are below a critical size [12] [13] and rapidly, e.g. $N_i \approx$ 5% N_f [14]</td></tr>
<tr><td>mostly at eutectic Si [13,15,16]</td><td>at Fe intermetallics when Fe content ↑ (0.1 to 0.7wt.%) [8]
But, Fe content ↑ (0.25 to 0.58wt.%) has no influence [13]</td><td rowspan="2">at Cu intermetallics in Cu-rich alloys (≥3wt.%) [15]</td></tr>
<tr><td rowspan="2">Cracks propagate (N_p)</td><td rowspan="2"></td><td colspan="2">through a network of hard particles:</td></tr>
<tr><td>Si particles [12,17] that fail by debonding [14] or fracture [9] inducing intergranular cracking and cleavage [10]
But, short cracks may avoid Si particles [19]</td><td>Fe [18] and mostly α-Fe intermetallics when Si particles are globular [19]
But, short cracks may be arrested by plate-like intermetallics [20]</td><td>Cu intermetallics in AlSi7Cu3Mg [18]</td></tr>
<tr><td>Total life (N_f)</td><td>N_f ↓with large pores [7–11] or with high porosity content [8]</td><td></td><td>N_f ↓ [8] with iron intermetallics
But, N_f can slightly ↑ when Fe content ↑ [20,21]</td><td></td></tr>
<tr><td rowspan="4">High temperature LCF or ThermoMechanical Fatigue (TMF)</td><td>Cracks initiate (N_i)</td><td>at pores at or near the surface [22] and below the surface at 250°C [23]. N_i depends on porosity content [24]</td><td></td><td></td><td></td></tr>
<tr><td rowspan="2">Cracks propagate (N_p)</td><td rowspan="2">By coalescence of cracks initiated at pores (>200°C) [25]</td><td colspan="3">through hard particles (TMF):</td></tr>
<tr><td>Si [3,26,27] particles (TMF) that fail by rupture at 200°C and by debonding at 275 and 350°C [28]</td><td colspan="2">Fe or Cu intermetallics (TMF) [3,22,26,27]</td></tr>
<tr><td>Total life (N_f)</td><td>N_f (TMF)↓ when the porosity content ↑ (from 0.5% to 2.75% in vol.) [29]</td><td>N_f (TMF) slightly ↑ when Si plates are turned into smaller and rounder fibrous particles [22]</td><td></td><td></td></tr>
</table>

Whatever the initiation site, LCF cracks at RT propagate through a network of hard particles where eutectic Si prevails [12,17]. Although acicular Si particles aligned with the loading axis [9,17] and clusters of Si particles [17] seem more likely to break, the influence of the particle morphology is still unclear: an alloy with a spheroidized eutectic Si has a lower LCF strength than the same alloy without spheroidisation and with a coarser microstructure [14]. Although present in the LCF crack path [18], Fe and Cu intermetallics are rarely studied. In a Sr-modified AlSi7Mg0.3-T6 alloy with globular Si particles, fatigue cracks rather propagate through α-Fe intermetallics (Table 1). Hence, in the early stages of fatigue, a crack may even avoid Si particles (Table 1).

If experimental studies on Al-Si alloys in RT LCF are rare, those in LCF at high temperature are even scarcer.

The thermal fatigue life decreases when the SDAS increases with more evidences of cleavage in the fracture surface [22]. However, as the SDAS scales with porosity and size of Fe intermetallics [22], this lifetime reduction could not be attributed to a single microstructural parameter.

At temperature above 120°C, creep-type damage mechanisms are activated but, when present, porosity still controls crack initiation and can help crack propagation through coalescence so that porosity content influences fatigue life (Table 1).

In TMF, cracks also grow through hard particles. Si particles failure mechanisms depend on the temperature and their influence of the fatigue life depends on their morphology (Table 1).

When available, in-situ observations during TMF are limited to the surface and generally obtained during interrupted tests to monitor surface crack growth [13,30]. In-situ X-ray tomography observations during LCF tests revealed crack initiation at subsurface pores that is thus undetectable from the surface during most of the fatigue life both at RT and at 250°C (Table 1).

To interpret such mechanisms, Finite Element Method (FEM) calculations with either a simplified microstructure based upon 2D observation or a more realistic microstructure from X-ray tomography were used in the literature to analyse the evolution of stresses and strains heterogeneity at the microscale with various microstructural parameters at RT (Table 2). The matrix is always assumed elastoplastic with non-linear hardening and the hard particles linear elastic.

Table 2: Investigated parameters in FEM calculations to study stress heterogeneity in Al-Si alloys at a microstructural scale

		Simplified microstructure (2D)			Realistic microstructure (3D)		
		Eutectic Si	**Pores**	**Influence**	**Eutectic Si**	**Pores**	**Influence**
Monotonic tension		*Shape : round* [31,32], *elliptic* [31], *lamellar* [33] *Size* [34] *Aspect ratio* [34][31]		*When the size ↑, the maximum stress slightly ↓ in the particle & ↑* in the matrix *so that yield strength ↓.* *Particles elongated in the loading direction are more likely to crack*		[35–42]	The maximum tensile stress between a pore and the free surface depends on the pore's depth [39].
		elastic Si lamellae	& small (20µm) **rounded pores** [33]	Crack initiation & fracture of Si particles close to pores			K_t depends on size with little influence of morphology [38,41]
		Isolated inclusions or pores [43] *Shape*: circular or with sharp morphologies *Size*: diameter		At a given size, morphology has limited influence on local plastic shear strain hence on crack nucleation.Size is more important than shape.			The largest K_t occur at high curvature areas of microshrinkages [35,36,40].
HCF		Al dendrite arm surrounded by eutectic Si	with and without a **spherical pore** [32]	A pore near the surface ↓ fatigue strength			crack nucleates where $K_t \geq 4.5$ [42]
LCF	**RT**				sub-volumes centred on single elastic Si particles [44]	[11]	Si particles with complex shape or aligned with loading direction are more harmful [44]
	HT					[23]	Cracks initiate at the pores hot spots with the highest equivalent plastic strain [11] [23]

Numerical simulations with 2D FEM models considering pores with model shapes , often spherical, were carried out to study their influence on stress fields in monotonic tension [33] or in HCF [32]. A pore near the surface reduces fatigue strength as it increases the stresses and plastic strains around Si particles at its tip [32]. Besides, the stress concentration induced allows crack initiation and fracture of surrounding Si particles and then dictate the crack path [33]. In monotonic and cyclic 2D simulations the pore shape has limited influence on the maximum value of the plastic shear strain (an indicator of the crack initiation driving force) at the edge of the pore whereas a four-fold increase in the pore diameter doubles the plastic shear strain. Therefore, the pores size is more important than its morphology for crack nucleation.

The influence of Si particles in monotonic tension or in HCF was also studied with FEM calculations on 2D simplified microstructures with elastic Si particles with various shapes, size, orientation, spacing and clustering (Table 2). Si particles generate a stress concentration in the adjacent matrix [33]. When the particle's size increases, the maximum stress in the particle slightly decreases while that in the matrix increases leading to a lower yield strength [34]. Particles with a high aspect ratio [34] elongated in the loading direction [31] support higher computed stresses than circular particles hence they are more likely

to crack. The shape has less influence on the stress within the matrix than the failure state of the particle [43]. Damaged particles generate a stress concentration in the surrounding matrix, which depends on their shape and orientation, and that is transmitted on the intact particles nearby. A broken particle still bears a significant fraction of the redistributed local stress field whereas the stress redistribution in the matrix is higher around a debonded particle [31]. Once the effective stiffness of the matrix decreases due to particles failure and yielding, the stress in the particles, hence the risk of particles cracking, increases [34]. When cracks have initiated in the matrix near damaged particles, their growth depends on the Si particles distribution [31]. The presence of Fe intermetallics, large Si particles and a small distance between these particles can locally increase stress/strain concentration [32].

X-ray tomography provided more realistic microstructures that could be used as input to this type of studies. 3D FEM model using real pores morphology (Table 2) enabled to compute local stress concentration factors K_t under monotonic tension assuming an elastic matrix [35–42] or to compare the cumulative equivalent plastic strain field after three LCF cycles with crack initiation site, first, at RT assuming an elastoplastic matrix with nonlinear isotropic/kinematic hardening model [11] then, at 250°C assuming an elasto-viscoplastic matrix [23]. Indeed, the computed K_t is a good indicator of the nocivity of a pore with HCF crack nucleating in areas where K_t is high [42]. Some authors stated that pores with the same Feret diameter have similar K_t with little influence of their morphologies [38,41] whereas computed stress fields on microshrinkages show that the largest K_t values occur at high curvature areas (hot spots) [35,36,40]. In LCF [11], a cyclic FEM computation of the pores in an elastoplastic matrix has proved that cracks indeed initiate at the microshrinkage hot spots with the highest computed equivalent plastic strain.

Analysis of the influence of realistic hard phases particles on strain fields is rare. High resolution tomography images acquired in-situ during a RT LCF test on an AlSi7Mg0.3 allowed analysing the effect of Si particle volume and orientation on rupture [44]. Teranishi *et al.* [44] built FEM models from tomographic data by considering a sub-volume centred on a single elastic Si particle in an elastoplastic matrix. Morphological analysis of the particles that break shows the harmfulness of a complex shape with thin portions, a locally high volume-fraction, and a small angle between major axis and loading direction. Besides, intact, or late breaking particles have high values of maximum equivalent plastic deformation while early breaking particles have high values of principal and hydrostatic stresses. However, discrimination by morphological parameters is not obvious. Larger particles seem more likely to break as

their aspect ratio and their angle with respect to the loading axis decreases. Yet, the study of the influence of the neighbourhood, i.e. pores, and hard particles, would be necessary for a more accurate estimation of the stresses in a given Si particle.

In summary, as contradictory experimental evidences and the lack of experimental data acquired in-situ and in the bulk do not allow a full understanding of the role of particles morphology, size, or orientation on crack initiation and propagation, some FEM simulations of model or realistic microstructures were performed. These studies have several limitations. First, they require knowledge of the constitutive law of the microstructural constituents. For the Al matrix containing Si particles at RT, a simple elastic behaviour can be assumed for rigid particles, but remains impossible for the intermetallics especially at high temperature. Therefore, three-dimensional experimental studies using X-ray tomography and Digital Volume Correlation (DVC), which are relatively recent techniques, are necessary to understand the influence of hard particles that are often not of ideal shape, as assumed by FEM analysis, but form complex clusters [45–47]. Above 150°C, the matrix behaviour changes and, at high temperature, damage of eutectic Si may dominate over that of intermetallics [30] but the influence of morphology is still a matter of discussion [22][24]. Consequently, the state-of-the-art shows that the criticality of the various hard particles with respect to LCF remains an open question especially at high temperature.

In this work, in order to clarify the role of the microstructure in high temperature LCF of cast Al-Si alloys, we performed in-situ observations under high resolution X-ray tomography during isothermal LCF tests at 250°C using the in-situ high temperature test rig presented in [48]. The tomographic images obtained at different number of fatigue cycles were analysed first qualitatively to have a comprehensive analysis of the damage scenario. Then, the strain heterogeneity at the scale of the microstructure was computed with DVC. The analysis of the strain fields, measured at an unprecedented spatial resolution, provides the cumulative local von Mises strains before failure for the different phases and it conducts to local Manson Coffin curves for fatigue crack nucleation. Besides, the evolution of local strains within various particles with the number of cycles allowed us to draw a hierarchy of the strain to failure among the different hard phases namely, eutectic Si, Cu and Fe intermetallics.

2 Experimental

2.1 Material and specimens

The material used to manufacture cylinder heads is a cast AlSi7Cu3Mg (A319) Al-Si alloy with the chemical composition shown in Table 3. Cylinder heads cast with the LFC process were overaged during 500 h at 250°C to obtain stabilized microstructure and the targeted mechanical properties. The resulting microstructure (Figure 1) is typical of hypo-eutectic cast Al-Si alloys: an Al dendritic structure with pores and hard inclusions, i.e. eutectic Si, Fe intermetallics and Cu containing phases, in the interdendritic space.

Table 3: Composition of the AlSi7Cu3Mg alloy in weight %

Si	Fe	Cu	Mn	Mg	Ni	Zn	Ti	Cr	Al
7.30	0.10	3.45	<0.004	0.31	0.048	<0.02	0.1	<0.012	Bal.

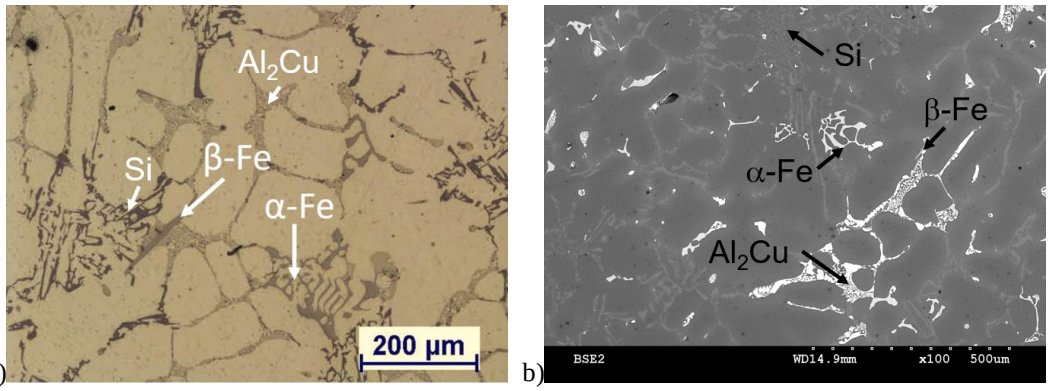

Figure 1: Microstructure of LFC AlSi7Cu3Mg observed with (a) optical microscope and (b) scanning electron microscope

The slower cooling rate of LFC as compared to DC process increases the SDAS (≈ 75µm) and the size of the pores and different phases present in the alloy compared with DC casting.

To obtain samples with a microstructure representative of the inter-valve zone, i.e. the critical area for TMF, small dumbbell-shaped specimens (Figure 2b and c) were extracted from the cylinder heads by Electro Discharge Machining (EDM) (Figure 2a).

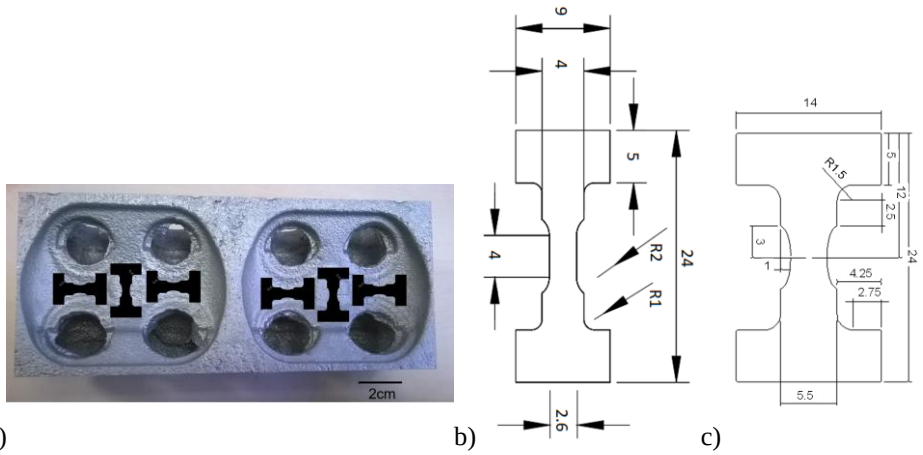

a) b) c)

Figure 2: Fatigue specimens: (a) location of the specimens in the cylinder head and geometries of (b) A4 and C5 (thickness 2.6 mm) and (c) LE7 (thickness 3.5 mm) specimens with dimensions in mm

All specimens were mechanically polished (SiC paper down to grit 4000 followed by polishing up to ¼ µm in a diamond solution) to remove the EDM affected layer of about 200µm, and to decrease the risk of surface crack initiation. After polishing, the cross section is 2 × 2 mm^2 (samples A4 and C5 hereafter) or 3 × 3 mm^2 (sample LE7); larger specimens were used to obtain a longer crack propagation.

A preliminary characterization by laboratory X-ray microtomography was performed on the ISIS4D[4] X-ray Computed Tomography platform with an 80kV acceleration voltage. The scan was made at a medium resolution with a voxel size of 5µm and an acquisition time per image of 500ms. On the one hand, these medium resolution images permit to select suitable samples and observation areas regarding pores size and location. Indeed, pores located in areas of high stress concentrations such as fillet can cause premature failure of specimens outside the field of view. On the other hand, the obtained images allow characterizing in 3D the population of defects in the specimen gauge length and obtaining a 3D mesh of the porous aluminium matrix in order to compute the associated strain fields using FEM with Abaqus software; More details in the mesh generation from tomography images are given in [11]. An

[4] https://isis4d.univ-lille.fr/

elastoplastic model with isotropic hardening, which was identified from a monotonic tensile curve of the studied alloy at 250°C, was used and a uniform displacement was applied on the upper and lower part of the 3D mesh to yield a macroscopic strain of 0.4%. Analysis of the strain fields obtained at the successive iterations of this computation allowed to select the iteration that yields a plastic strain area that is large enough to induce crack initiation in the observation area but that remains smaller than the specimen's width in order not to induce ductile failure. The macroscopic strain so identified was then used to define the stress or load applied at the maximum of the first cycle in the in-situ LCF tests using the cyclic stress-strain curve of the alloy. Considering the different pores distribution and specimens' geometry, the applied stress selected may differ among specimens.

2.2 In-situ fatigue setup

To observe and follow the damage micromechanisms in bulk and in-situ, isothermal LCF tests were performed at ID19 beamline at the European Synchrotron Facility (ESRF, Grenoble in France). The samples were loaded using a uniaxial in-situ fatigue test rig [23] developed at MATEIS laboratory. To perform LCF tests at high temperature, a furnace with four halogen lamps, described in [48], was added to this test rig by the "Centre des Matériaux" laboratory. Tests at 250°C were performed at a frequency of 0.1Hz, a stress ratio $R \simeq 0.1$ and with a maximal force, which was adjusted by an imposed displacement of the lower grip.

Tomographic scans were acquired in pink beam mode ($E \simeq 35$keV) with a CMOS PCO Dimax detector (2048×2048 pixels^2) at 2.75µm voxel size. At high temperature, the material has a partly viscous behaviour that induces stress relaxation under displacement control. Hence, to reduce as much as possible this effect, fast scans (45s duration for 2,000 radiographies) under maximum load were recorded after a dwell time sufficiently long to reach macroscopic stress stabilization ($\simeq$ 5min). The phase contrast provided by the coherent synchrotron X-ray beam enables to distinguish Al from Si despite their close X-ray attenuation coefficient but it also induces spurious artefacts at the borders of pores and microstructural constituents. Therefore, volume reconstruction relied on a Paganin algorithm [49] to improve contrast.

2.3 High resolution strain field calculation

3D displacement fields were computed with YaDICs [50], an in-house open-source software for Digital Image Correlation. YaDICs allows the use of many transformations to adapt to the tests performed. These can be either local using inter-correlation and integrated local block correlation, or global with a finite element basis. In the present study, an optical flow method on a finite element basis was retained. Details about the correlation sequence that was chosen to achieve 3D displacement fields with a cubic element of 4×4×4 voxels (11×11×11 µm) can be found in [50] together with uncertainty analysis.

A high spatial resolution of the displacement fields is necessary to analyse their heterogeneities at a spatial resolution close to the size of the microstructure. Figure 3 shows this 3D microstructure, which was characterized using a high resolution tomography volume with a 1.6µm voxel size, in a volume of about $1mm^3$: the hard phases have many connected branches and form an intricate network so that a smaller subvolume was needed for the 3D rendering of iron intermetallics (Figure 3c) and eutectic Si particles (Figure 3d) to distinguish their morphology. For such complex networks, a granulometry analysis [51] is the most appropriate method to rank the microstructural constituents by their size distribution (Figure 4): the eutectic Si phase is the thinnest one (average≃5µm), the Fe intermetallics phases have roughly the same thickness peak but with a distribution that extends towards larger values (average≃9µm), finally, the Cu intermetallics phases are the thickest hard phases (average≃13µm). Other constituents, i.e. Al dendrites and pores, have thicknesses ten times higher, with average values of 67 and 80 µm respectively. Please refer to [11] for a full description of the 3D pores in this material.

As strain is computed from the gradient of the displacement field, its spatial resolution (shown as a green square in Figure 5) is based on a volume 27 times larger than the cubic element size (in red in Figure 5) on which DVC is based. For thin particles, such as eutectic Si (Figure 4), the DVC volume element, in which strain is calculated, will thus always include the selected particle but also Al matrix. Only in the thicker Cu intermetallics (Figure 4) could “true” local strain measurements be obtained within the particles. However, Cu intermetallics, either with the fine eutectic or blocky form are part of an Al-Cu eutectic (see Fig. 17a and b in reference [52]) and if the Al eutectic is not resolved on the tomography

images (see Figure 5), it can still influence the measured local strain. Therefore, Al will affect the measurement for the three hard phases.

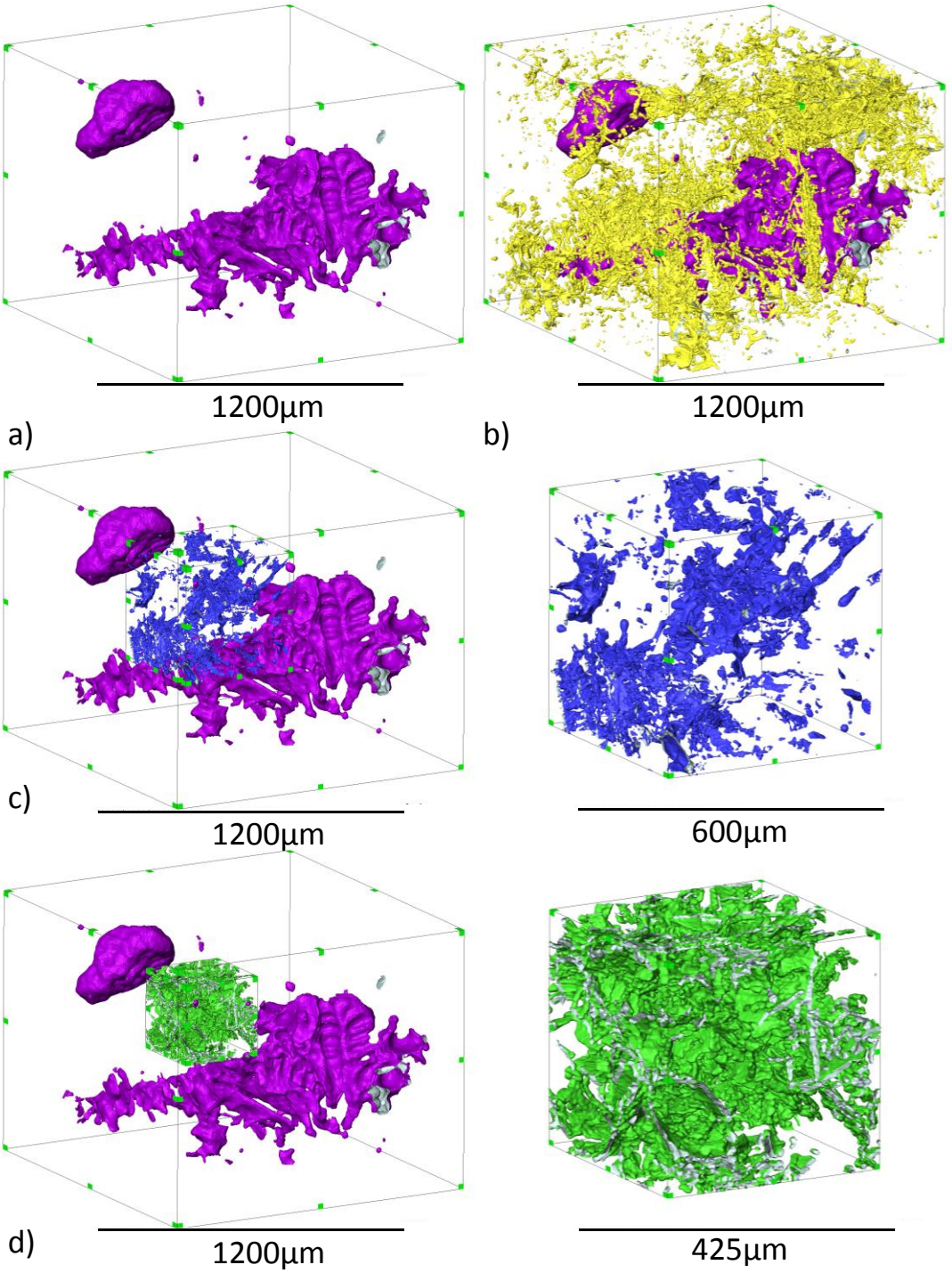

Figure 3: 3D microstructure of AlSi7Cu3Mg using high resolution tomography (voxel=1.6µm) showing (a) pores and hard phases: (b) Al_2Cu, (c) Al(Fe,Mn)Si and (d) Si; For the thin Al(Fe,Mn)Si

and Si phases, zoomed regions on the right hand side of (c) and (d) give an insight into the network complexity.

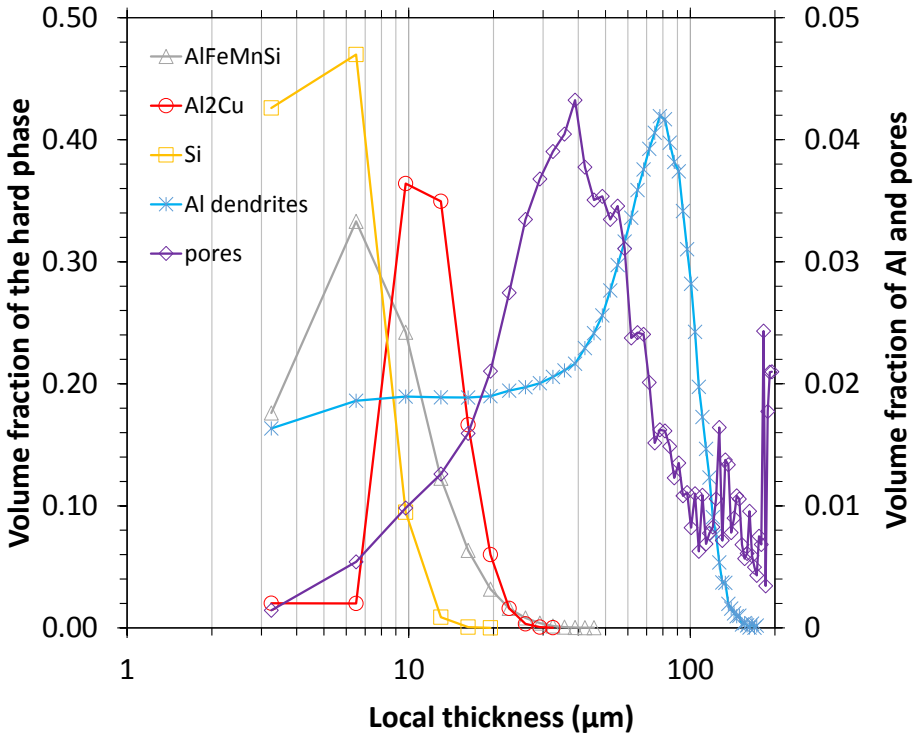

Figure 4 : Thickness distribution in volume fraction of the considered phase; Analysis is based on tomography images with a 1.6 µm voxel size hence objects thinner than 3.2 µm are not included.

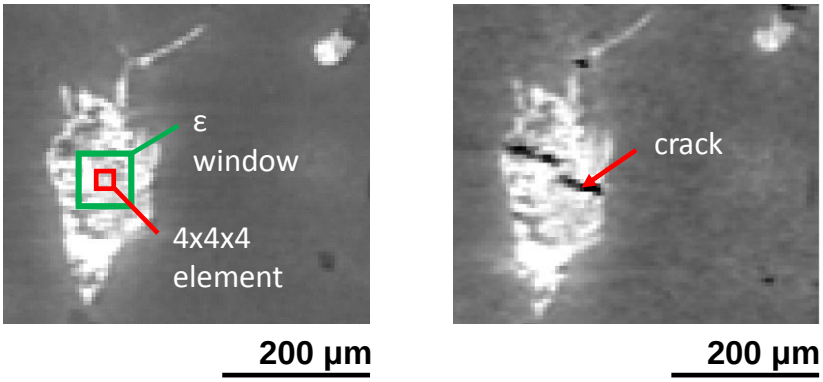

Figure 5: Illustration of the spatial resolution of local measurement (on the left, in red for displacement and in green for strain) in an Al-Al_2Cu particle that eventually breaks (on the right)

For several particles belonging to the three hard phases, the local strain was monitored until the particle failed. First, the coordinates of a point at a particle fracture were identified on a tomographic slice perpendicular to the plane of the crack at a number of cycles N (Figure 5 right-hand side). Then, an ImageJ macro was used to retrieve the value of the cumulative von Mises strain at this point (Figure 5 left-hand side) for all scans recorded when the particle was still intact; the cumulative strain at N cycles was obtained from DVC between the reference image at the minimum load of the 1^{st} fatigue cycle and the deformed image at the maximum load of the N^{th} cycle.

3 Results

3.1 Damage mechanisms

Three in-situ fatigue tests were conducted and analysed. Specimens C5 and A4, loaded at a maximum stress of 70MPa, failed after 50 fatigue cycles, while sample LE7, loaded at 65MPa, failed after 1,800 cycles. In most of the fatigue tests, a crack initiated during the loading part of the 1^{st} cycle near a large micro-shrinkage, i.e. in an area of high stress concentration due to the pore's shape, usually below the sample surface. Due to the similarity between samples C5 and A4, only samples A4 and LE7 are discussed in what follows. Although X-ray tomography was performed with a medium resolution (voxel size = 2.75µm), it allowed detecting microcracks resulting from the failure of hard particles. Figure 6 compares a Scanning Electron Microscopy (SEM) image of the specimen surface post-mortem with a tomography slice before specimen failure. Both techniques enable to detect the same mechanisms: broken Al_2Cu intermetallics and microcracks at failed eutectic Si particles. Phase contrast allows the detection of microcracks and of the Si particles. Hence, X-ray tomography images obtained at different numbers of cycles are considered reliable to analyse the fatigue mechanisms. However, as the distinction between fracture and debonding of hard phases particles could not be done in the tomography images, in what follows, the generic term of failure is used hereafter to describe any particle damage that led to the creation of a microcrack.

In the two analysed samples, cracks initiated at the microshrinkage with the maximum Feret diameter: 1050 µm for sample A4 and 781 µm for sample LE7. In sample A4, after initiation during the first

loading, an Al_2Cu particle located near the largest microshrinkage (pore tip marked "1a" in Figure 7c) failed and then propagation occurred along the Si phase. After 5 cycles, other microcracks in Si particles were observed around pore tip "1b", which actually belongs to the same microshrinkage as pore tip "1a". After 5 cycles, the microcracks already nucleated at eutectic Si particles (circled area in Figure 7c) open up more while newly formed microcracks multiplied in the zone that links adjacent pores 1 and 2 (see Figure 7c) until they enlarged and coalesced to form a single cavity, which led to the sample fracture.

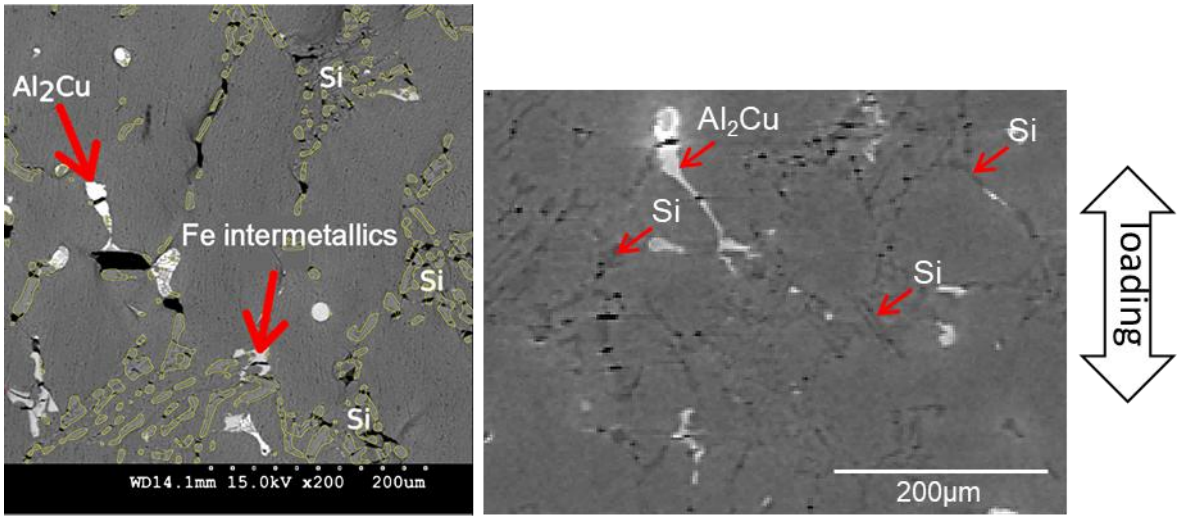

Figure 6: Comparison of broken hard particles observed post-mortem at the surface with SEM where the Si phase contour is underlined in yellow (on the left) and in the bulk with X-ray tomography at the last scan before failure (on the right). The two images are shown at comparable magnification.

The damage scenario was the same for LE7 despite a longer fatigue life. Fatigue cracks initiated close to the largest subsurface pore via the failure of hard inclusions: mostly eutectic Si although broken Al_2Cu and iron intermetallics were also observed. EDS analysis of the fracture surface at 250°C (see p165 in reference [53]) and at RT [54] confirmed that the surface fraction of Si phase dominates ($\simeq$ 29%) compared to Al_2Cu ($\simeq$ 7%) and AlFeMnSi ($\simeq$9%). More microcracks at damaged hard inclusions were observed when the number of cycles increased until they coalesced to form larger cracks that rapidly led to failure of the specimen.

The analysis of the surface fractions occupied by either fracture or decohesion in the different hard phases showed that the decohesion/fracture ratio is higher for Si at 250°C (≥ 4.4) than at room temperature (≥ 1.3 [57]) both on the whole fracture surface and on the crack initiation zone. At 250°C, the post-mortem SEM analysis also confirmed that Si damage largely prevailed whereas Cu intermetallics were rarely present on the fracture surface contrary to the RT results while Fe intermetallics showed the same particles fracture/decohesion ratio as at RT.

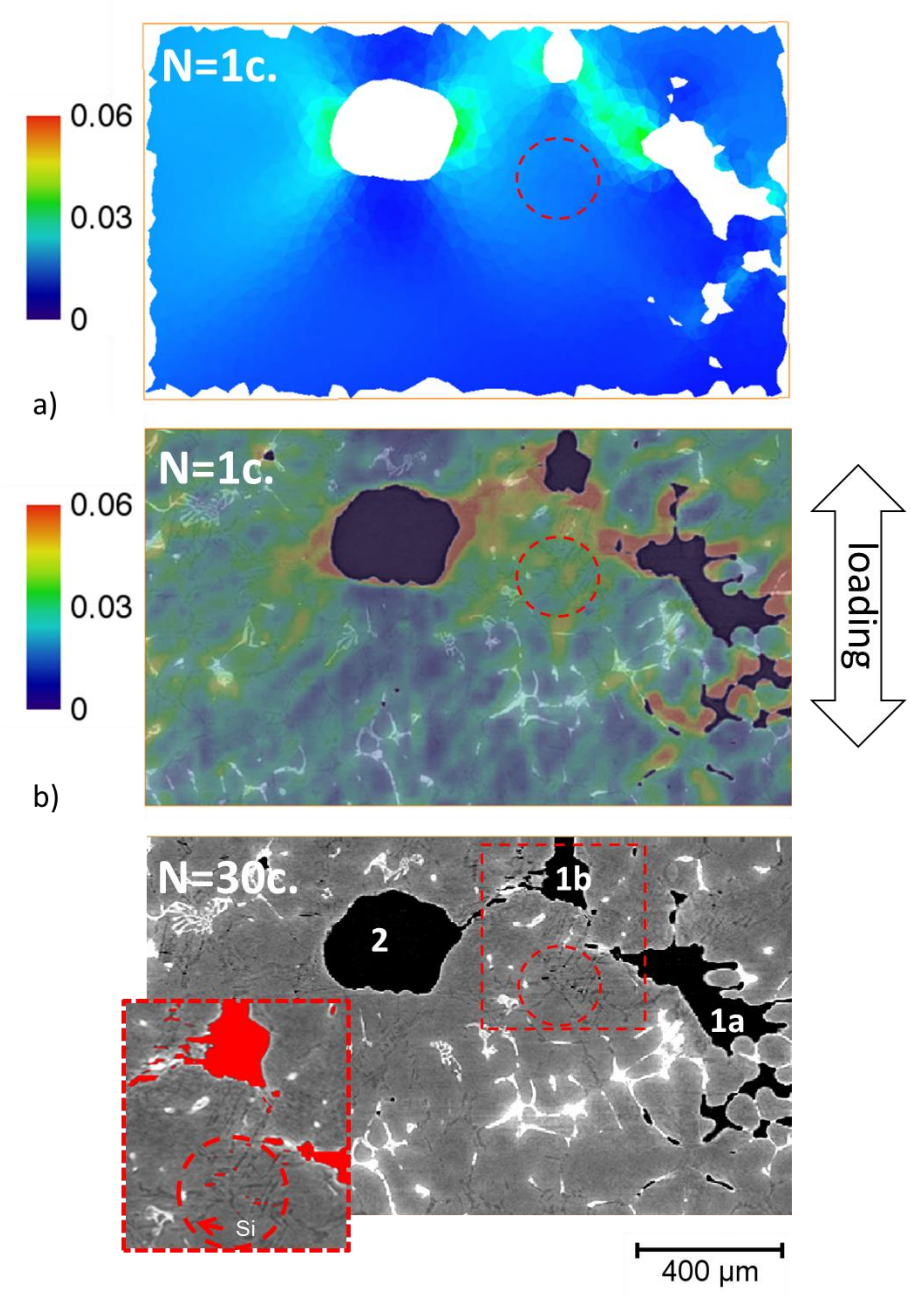

Figure 7: Strain field at the 1st cycle (sample A4) in one slice about 700µm below the specimen surface: (a) equivalent plastic strain computed from FEM for an elastoplastic porous model and (b) von Mises total strain measured from DVC; A zone containing microcracks after 30 cycles is encircled in red in the corresponding tomographic slice in (c); A focus in a rectangular area that joins the pores and presents numerous microcracks at 30 cycles allows to highlight the microcracks in red and the Si particles (arrow)

3.2 Strain field heterogeneity

Figure 7a shows one slice within the 3D equivalent plastic strain field, which was computed with FEM assuming an elastoplastic homogeneous material, and the corresponding slice (Figure 7b) in the ε_{vMises} total strain field from DVC at the first fatigue cycle for A4 sample; the microtomography images of the microstructure, shown in Figure 7c, were superimposed on this field to compare the crack path with the local deformations. In the equivalent von Mises strain field computed from DVC in Figure 7b, a strain localization can be observed on a relatively large area between the two pores (red circles) before crack initiation. Near Pore 1, a locally higher ε_{vMises} strain corresponds to a crack that initiated at the tip "1a" from eutectic Si; after 30 cycles, the crack has opened and propagated through an Al_2Cu intermetallic (Figure 7c).

The comparison of the computed equivalent plastic strain field with the measured von Mises strain field at the same cycle shows a good correspondence between the shape of the highly strained area that links the pores although with much higher experimental values. However, areas with large experimental strain values also existed outside the pores strain localization area computed with FEM (see the dotted red circle in Figure 7). These zones are observed at hard particles with strain values that may increase with the number of cycles up to particles failure. Microcracks at Si particles were indeed observed to nucleate far from the strain concentration area induced by pores. Therefore, a detailed analysis of the evolution of strain at some particles until failure has been performed.

3.3 Analysis of local strain at hard particles

Deformation at the scale of the hard particles was analysed following the DVC strain measurement method described in section 2.3. As explained before, at the spatial resolution of DVC, Al influences the strain measured in the three hard phases. Hence hereafter the measured strain is attributed either to {Al+Al_2Cu}, {Al+Fe} or {Al+Si} whether the studied hard phase particle belongs to Cu intermetallics, Fe intermetallics or eutectic Si respectively. Selected points on some failed particles were monitored in tomographic slices, as shown in Figure 8 for a Cu intermetallic particle in sample A4. The evolution with cycles of the ε_{vMises} strain at these points was measured. The maximum strain occurred where the particle

failure is observed on the following scan as shown by the projection of the von Mises strain field at 6 cycles on a particle that appears broken at 30 cycles (Figure 8); the particle has failed between 6 and 10 cycles but the crack was better revealed at 30 cycles. Hence, in this example, the strain at or before failure corresponds to the strain measured at 6 cycles.

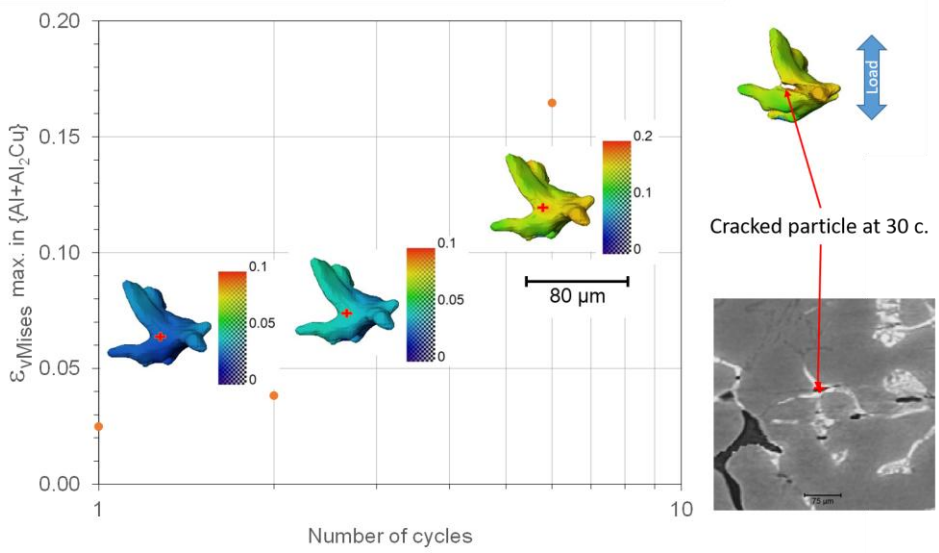

Figure 8: Evolution of the ε_{vMises} strain within one particle with the number of cycles up to the last cycle where the particle is intact. A red cross on the 3D particle, which is coloured by the strain field at the corresponding cycle, indicates the measurement location. On the right-hand side, the broken particle after 30 cycles (sample A4) is shown in 3D and within a 2D reconstructed slice.

The same study was carried out at several points (over ten) where a crack was observed for the three hard phases. Figure 9 shows the evolution of local strains in several {Al-Al_2Cu} particles that failed after 200 cycles in sample LE7. As sample LE7 had a much longer fatigue life (1,800 cycles), particles broken after only 300 cycles were selected and studied. This allowed to study particles far from a growing crack and its plastic zone. At 200 cycles, the von Mises strain values before failure show an important scatter among the selected particles.

Figure 10 shows the average strain variation in the three types of hard particles before failure. For both samples, local strains gradually increased with the number of cycles until failure whatever the particle and, for each hard phase, the strain dispersion at a given number of cycles is significant as shown by the

standard deviations reported as error bars in Figure 10. However, a hierarchy emerges between the three hard phases.

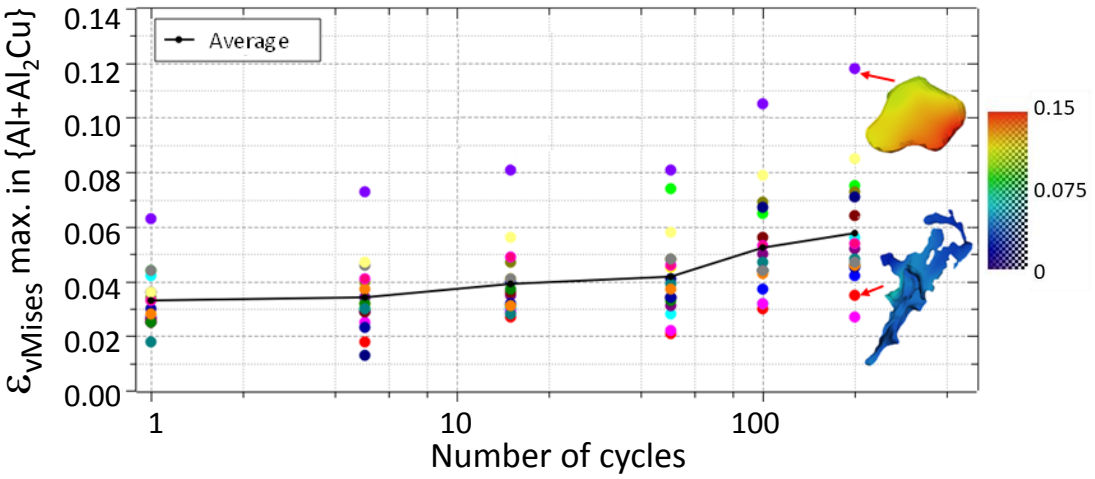

Figure 9: Evolution of the ε_{vMises} strain within several {Al+Al$_2$Cu} particles with the number of cycles up to failure (sample LE7). A 3D rendering shows the strain localization at 200 cycles for two particles.

At a given cycle, {Al+Al$_2$Cu} particles show the highest strains accumulation while being intact. {Al+Fe} particles have slightly lower values while {Al+Si} are even below. The strain evolution for the three types of hard particles follows the same hierarchy and shows consistency between specimens LE7 and A4.

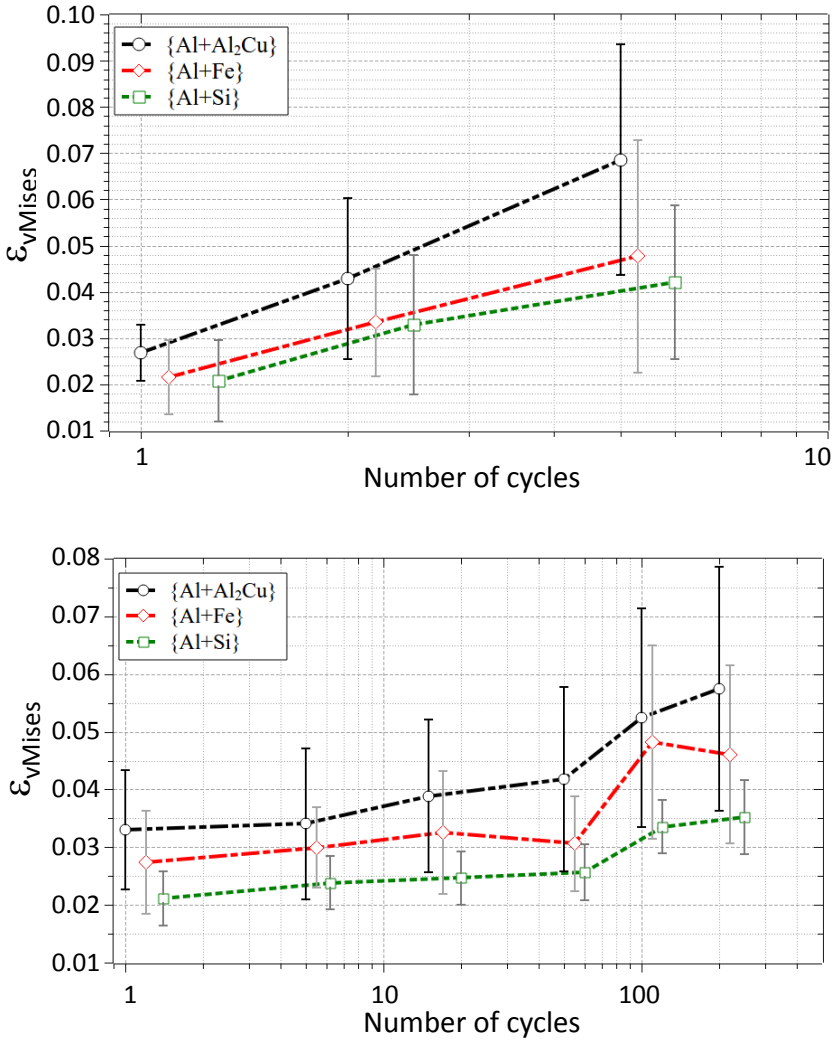

Figure 10: Mean evolution of the ε_{vMises} strain before failure for the three types of hard particles in specimen A4 (top) and LE7 (bottom) that failed after 50 and 1,800 cycles, respectively; the three series are shifted on the abscissa to improve readability of the figure.

4 Discussion

4.1 Influence of temperature on damage mechanisms

At RT [11] and at 250°C, the fatigue crack initiation mechanisms observed during our tests are identical. The first cracks often initiate before reaching the maximum load of the 1st cycle, i.e. during the first pull. Crack initiation mechanisms in fatigue are therefore not different from those in monotonic

tension [11,55]. The crack initiation site was either one or several subsurface large micro-shrinkages with a tortuous morphology. These complex shapes resulted in a strain localization evidenced by both DVC and FEM. Crack initiation also resulted from the presence of hard particles located near pores or near other stress concentrations, e.g. the specimen fillet [11]. Propagation then followed the hard phases where an increase in the cumulative von Mises strain, measured by DVC, was found before crack detection.

At 250°C, significant microcracking of the eutectic Si appeared at the 1st cycle (Figure 7 bottom). Eutectic Si showed massive multi-cracking in areas close to the pores in the region of the sample where the final fracture occurred but also elsewhere (see e.g. the circled area in Figure 7). However, microcracks or cavities generated at Si particles away from the pores or from a stress concentration did not coalesce to form a macrocrack. This is consistent with the observation of Joyce [30] who reported that Si fracture does not necessarily induce (macroscopic) crack initiation.

Since Si is the hard phase with the highest volume fraction, the number of failed Si particles in the fracture surface is expected to be higher than for other phases like at RT. Besides, the morphology of Si may explain why a fracture at one location of a network led, by a load transfer on the unbroken ligaments via the matrix, to a greater stress and therefore a probable fracture of these ligaments or of the adjacent unbroken particles. Post-mortem analysis has underlined the importance of Si decohesion at 250°C compared to RT results in agreement with the change of failure mechanisms induced by temperature as reported in [28].

At high temperature, the mechanical properties (Young's modulus and hardness) of the matrix decrease more markedly than for rigid inclusions and among the hard particles, Si is the phase that maintains the highest hardness up to 350°C [56,57] thus accentuating the Al/Si matrix incompatibilities and the damage of the Si particles.

Another explanation given in the literature for the fracture/decohesion of Si is the presence of residual stresses due to thermal expansion mismatch between matrix and particles. Indeed, when isothermal high temperature fatigue tests are interrupted to measure fatigue cracks growth, Joyce [30] observed that this “thermal cycle” induced numerous broken Si particles and reduced fatigue life compared to uninterrupted tests [30].

Yet, in the present study, tomographic scans taken before and after heating to 250°C, while the specimen was held at the minimum load before any fatigue cycles, did not show any increase of the

number of damaged particles so that damage cannot be attributed to one thermal cycle but rather to isothermal fatigue where local residual stresses could play a role. The casting process induces tensile residual stresses in the matrix and compressive residual stresses in Si particles that become tensile upon heating beyond 130°C, facilitating the failure of Si according to [58]. However, at 250°C, no residual deformation was measured in Si by Pyzalla *et al.* [59] maybe because of the thermal relaxation of the residual stresses that might still increase the effective stress in the Si particles as compared to RT while it decreases it in the matrix for the same nominal stress hence promoting massive Si failure.

It is likely that in the present study the massive failure of Si particles is due to the elastic/plastic mismatch with the matrix whose role in Si particles fracture is already suggested by Gall et al. [31] at RT. At 250°C, this mismatch increases and probably leads to an increased propensity to particles failure.

4.2 Measured vs computed strain in a homogenous material

Although the strain field obtained from FE simulations in Figure 7 matches the distribution of the *measured* strain in the neighbourhood of pores, it underestimates the values of the measured strains. Based on tomography images, another FEM computation was performed on a realistic 3D mesh of sample A4 taking into account the pores in a homogeneous matrix by Dezecot *et al.* [23,60]. Contrary to the computation presented in section 3.2, the loading was cyclic and the whole fatigue life, i.e. 50 cycles, was computed. Besides, the constitutive model was an elasto-viscoplastic Chaboche model rather than a simple elasto-plastic one. The aim was to assess the influence of pores on stress/strain concentration effects under cyclic loading; damage was not considered in the computation. The cumulative inelastic strain was averaged and followed with cycles in several spherical regions around the pores involved in the final failure. The computed maximum stresses/strains at pores were found to correlate well with the crack initiation sites observed.

One of these measurement areas ("SV4_R50" in Figure 10 of [23]) is close to the spherical Pore 2 shown in Figure 7. The local cumulative plastic strain is about 0.4% at the 1^{st} cycle, 0.5% at the 2^{nd} cycle and 1.07% at the 50^{th} cycle. Again, this is less than the average value of about 6% measured in an equivalent sphere in the von Mises strain field measured between the minimum of the 1^{st} cycle and the maximum of the 2^{nd} cycle although no crack was observed at this location so early in the LCF test. Hence,

computed strains obtained with a macroscopic constitutive behaviour law are consistently much lower than those measured. This large discrepancy between computation and measurement could be attributed to: (i) the elasto-viscoplastic constitutive model that underestimates the ratchetting, (ii) a homogenised matrix harder than the local Al matrix or, (iii) microcracks or particles failure that may occur early at the tip of pore and that are neglected in the computation, or any combination of those. Altogether this underlines the necessity to *measure strains* to get a better understanding of the fatigue behaviour of this complex microstructure.

4.3 Strains before failure of eutectic Si and intermetallic compounds

The studied AlSi7Cu3Mg LFC alloy does not behave like a homogeneous material but rather like a composite with a ductile Al matrix and intermetallic and Si reinforcements that are like very long fibres forming interconnected networks as shown in Figure 3. In a particle elongated in the loading direction, Saigal and Fuller [34] reported that the stress increases and that in the matrix decreases, fostering the rupture of the particle. The matrix then deforms plastically because of the ruptured Si. This is consistent with what we observed and it justifies the need to analyse the heterogeneous strain field in Figure 7 at a very local scale.

The hierarchy of strain levels evolution with cycles between the three families of hard inclusions in Figure 10 remains the same as those previously obtained at RT (see Fig. 52 in [61]). Interestingly, it matches the hierarchy of the hard phases' Young modulus measured by nanoindentation [56]. The fact that Si failure strain is the lowest one corroborates the early and massive cracking of Si particles as compared to Fe and Cu intermetallics. **Contrary to what we might expect from literature, in the present alloy the Fe intermetallics do not appear to be more deleterious to high temperature LCF than eutectic Si.**

For all phases, the scatter of the strain values before failure is large as revealed by the standard deviations (Figure 10). This scatter may have several causes. First of all, the brittleness of hard phases induces an intrinsic scatter in the local failure strength [62]. In the present study, dispersion could also be due to the low acquisition frequency of the scans, which led to inaccuracy in the real number of cycles at fracture and thus in the exact value of the strain at fracture. For example, the average strain before failure

of a particle broken at 300 cycles in sample LE7 (Figure 9 and Figure 10b) was estimated via the average strain at the point corresponding to the previously analysed scan, i.e. at 200 cycles, while failure may have occur anytime between 201 and 300 cycles. Furthermore, the spatial resolution of field measurements cannot be finer than the size of the speckle used for the correlation, i.e. the microstructure. Even DVC elements where one of the hard phases prevailed contained a fraction of Al matrix. The analyses could therefore not exclude measurements made on elements where the phase of interest is not predominant as such a restriction would prevent any local measurement in Si. Indeed, the few elements where Si is in majority may contain on average about 43% Al in volume so that the measurement includes not only the eutectic Si deformation but also Al deformation, i.e. eutectic Al and perhaps dendritic Al. The eutectic Al-Si constituent contains about 88% Al and 12% Si by volume and because of the low thickness of the Si phase, measuring the deformation of Si alone is impossible. For the eutectic Al-Al_2Cu, the volume fraction of Al in the eutectic constituent can be estimated at about 53% by considering a binary Al-Cu alloy. This lower ratio of Al in the eutectic Al-Al_2Cu combined with a thicker Al_2Cu phase implies that the local values in Cu intermetallics reflected less the behaviour of Al and more that of the intermetallics than in the Si case.

The main difficulty in validating our measurements is that there are no available data on the deformation of the hard phases above RT. As mentioned before, failure strength values do exist for Si at RT, but due to its inherent brittleness and the probability of having a defect in a "large particle", these values are highly scattered [62].

The scatter in failure strains among one phase may also come from the particle morphology as seen in the introduction. Several 2D FEM analyses [31,34,63] try to explain the behaviour of Si particles according to their morphology or distribution. Unfortunately, they are quite difficult to transpose to the 3D network morphology of Si in the present study (Figure 3) because only unconnected particles, isolated or in clusters, are considered whereas the interconnected architecture of the eutectic Si has a reinforcing effect due to load transfer between matrix and network.

When comparing the particles that fail at a given number of cycles, the strain before failure at RT tends to increase with increasing particle size and decreasing sphericity [61]. The same trend was observed at

250°C. Considering that large particles are more likely to belong to networks than smaller particles of larger sphericity, this observation could agree with those of Requena *et al.* [64] who find that an interconnected Si phase can withstand larger stress, hence a larger strain, than a Si phase whose interconnectivity has been destroyed by heat treatment. It was not possible to evidence any influence of particle/network orientation. More observations would be needed to confirm this point.

The particles showing the highest strain values at failure have longer fatigue lives regardless of the phase. This observation corroborates Teranishi's observation that intact or late-breaking particles have high values of maximum equivalent plastic strain [44]. Strain at failure is not independent of the number of cycles. Hence, by dividing the cumulative strain at failure by the number of cycles before failure for each studied particle, Manson-Coffin curves were plotted in Figure 11 assuming a linear evolution of the cumulative strain with cycles.

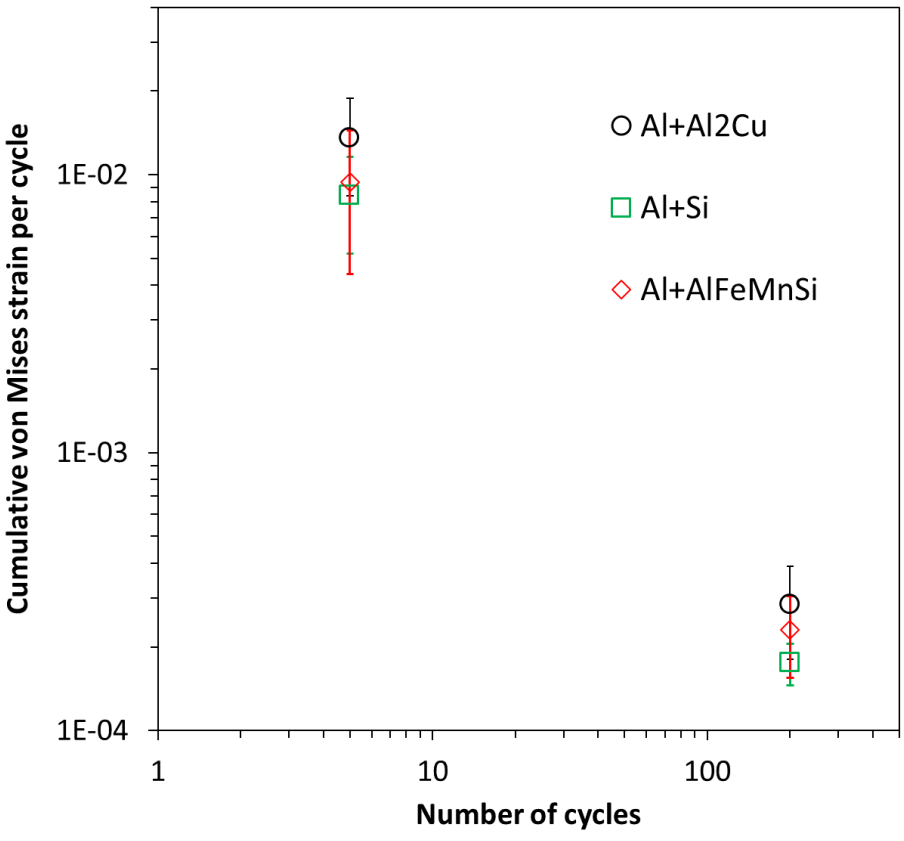

Figure 11 : Manson-Coffin curves of the different hard phases at 250°C.

To the best of the author's knowledge it is the first time that such values of fracture strains are reported for this type of alloy at high temperature.

No data are available in the literature to validate these local Manson-Coffin curves. The only available data in LCF at HT for this alloy come from LCF tests conducted at 250°C on macroscopic specimens of the same AlSi7Cu3Mg LCF material (aged 200h at 250°C) [65]. The "local" Manson-Coffin curves in Figure 11 present shorter fatigues lives compared to the macroscopic ones. This is consistent with the fact that they correspond to microcrack initiation while macroscopic curves do correspond to the specimen failure.

As shown in section 4.2 considering a homogeneous behavior fails to reproduce the local strains measured in LCF. Having local Manson-Coffin curves for the microstructural constituents is a first and necessary step to take into account the microstructural heterogeneity for any attempt of predictive computation.

5 Conclusions

In-situ LCF tests were performed at 250°C on a Lost Foam cast AlSi7Cu3Mg alloy and damage development was studied using synchrotron X-ray tomography. The 3D images obtained at different cycles and the fracture strain analyses carried out give new insights on fatigue damage both qualitatively and quantitatively.

The large microshrinkage pores control crack nucleation, by promoting failure of hard particles in areas of high strain localization due to their complex morphology. However, at 250°C, the failure of hard particles, mainly Si particles, occurs massively even at the 1st cycle. Damaged hard particles induce microcracks whose coalescence in the stress concentration areas of pores, lead to final failure. Contrary to the observation at room temperature, Si decohesion predominates over Si rupture at 250°C pointing at a possible change in damage mechanisms with temperature.

Considering a homogenous behaviour for the FE computation of the 3D strain field in the porous matrix, i.e. without considering hard phases, leads to a strong underestimation of the local strains close to pores even when a sophisticated constitutive behaviour model is used. While computation of a realistic AlSi7Cu3Mg microstructure is out of reach, the high spatial resolution of the 3D strain fields achieved with DVC has allowed to measure strains locally "within" the hard phases' particles of the microstructure

and to establish for the first time a hierarchy in the failure strain; in descending order: Al_2Cu intermetallics, iron intermetallics and eutectic silicon.

The local strain values measured allowed to propose a Manson-Coffin curve for each hard phase. Although efforts are still required to identify even more "local" values than those obtained, the quantitative data obtained in this study could feed models of the mechanical behaviour of these alloys at high temperature.

Acknowledgements

The authors wish to thank the ANR (Agence Nationale de la Recherche) MatetPro project INDiANA (ANR-12RMNP-0011) for funding the study on LFC Al-Si-Cu alloy. The ESRF (European Synchrotron Radiation Facility) is also acknowledged for providing beamtime on the ID19 beamline; Elodie Boller and Vincent Fernandez are particularly acknowledged for their help and advices with the Synchrotron tomography experiment. The ISIS4D X-Ray CT platform has been funded by International Campus on Safety and Intermodality in Transportation (CPER CISIT 2007-2013), the Hauts-de-France Region, the European Community, and the National Centre for Scientific Research. The authors gratefully acknowledge the support of these institutions.

The tests were made possible thanks to a high temperature test rig developed by Alain Koster suddenly disappeared in 2021 and to whom we wish to pay tribute.

References

[1] S. Shivkumar, L. Wang, D. Apelian, The lost-foam casting of aluminum alloy components, JOM. 42 (1990) 38–44. https://doi.org/10.1007/BF03220435.
[2] B. Kang, Y. Kim, K. Kim, G. Cho, K. Choe, K. Lee, Density and mechanical properties of aluminum lost foam casting by pressurization during solidification, Journal Of Materials Science And Technology-Shenyang-. 23 (2007) 828.
[3] S. Tabibian, E. Charkaluk, A. Constantinescu, A. Oudin, F. Szmytka, Behavior, damage and fatigue life assessment of lost foam casting aluminum alloys under thermo-mechanical fatigue conditions, Procedia Engineering. 2 (2010) 1145–1154.
[4] M. Riedler, H. Leitner, B. Prillhofer, G. Winter, W. Eichlseder, Lifetime simulation of thermo-mechanically loaded components, Meccanica. 42 (2007) 47–59.
[5] M.B. Grieb, H.J. Christ, B. Plege, Thermomechanical fatigue of cast aluminium alloys for cylinder head applications–experimental characterization and life prediction, Procedia Engineering. 2 (2010) 1767–1776.

[6] R. Molina, M. Leghissa, L. Mastrogiacomo, New developments in high performance cylinder heads: application of LHIP and SPLIT cylinder head concep, Metallurgical Science and Technology. 22 (2004) 3–8.
[7] Zhang, Chen, Poirier, Effect of solidification cooling rate on the fatigue life of A356.2-T6 cast aluminium alloy, Fat Frac Eng Mat Struct. 23 (2000) 417–423. https://doi.org/10.1046/j.1460-2695.2000.00299.x.
[8] D.O. Ovono, I. Guillot, D. Massinon, Study on low-cycle fatigue behaviours of the aluminium cast alloys, Journal of Alloys and Compounds. 452 (2008) 425–431.
[9] A.R. Emami, S. Begum, D.L. Chen, T. Skszek, X.P. Niu, Y. Zhang, F. Gabbianelli, Cyclic deformation behavior of a cast aluminum alloy, Materials Science and Engineering: A. 516 (2009) 31–41. https://doi.org/10.1016/j.msea.2009.04.037.
[10] H.A. Elhadari, H.A. Patel, D.L. Chen, W. Kasprzak, Tensile and fatigue properties of a cast aluminum alloy with Ti, Zr and V additions, Materials Science and Engineering: A. 528 (2011) 8128–8138. https://doi.org/10.1016/j.msea.2011.07.018.
[11] L. Wang, N. Limodin, A. El Bartali, J.-F. Witz, R. Seghir, J.-Y. Buffiere, E. Charkaluk, Influence of pores on crack initiation in monotonic tensile and cyclic loadings in lost foam casting A319 alloy by using 3D in-situ analysis, Materials Science and Engineering: A. 673 (2016) 362–372. https://doi.org/10.1016/j.msea.2016.07.036.
[12] D.-F. Mo, G.-Q. He, Z.-F. Hu, X.-S. Liu, W.-H. Zhang, Effect of microstructural features on fatigue behavior in A319-T6 aluminum alloy, Materials Science and Engineering: A. 527 (2010) 3420–3426. https://doi.org/10.1016/j.msea.2010.02.055.
[13] P. Huter, P. Renhart, S. Oberfrank, M. Schwab, F. Grün, B. Stauder, High- and low-cycle fatigue influence of silicon, copper, strontium and iron on hypo-eutectic Al–Si–Cu and Al–Si–Mg cast alloys used in cylinder heads, International Journal of Fatigue. 82, Part 3 (2016) 588–601. https://doi.org/10.1016/j.ijfatigue.2015.09.015.
[14] J. Stolarz, O. Madelaine-Dupuich, T. Magnin, Microstructural factors of low cycle fatigue damage in two phase Al-Si alloys, Materials Science and Engineering A. 299 (2001) 275–286. https://doi.org/10.1016/S0921-5093(00)01428-3.
[15] P. Huter, G. Winter, M. Schwab, P. Renhart, S. Oberfrank, F. Grün, B. Stauder, Comparison of microstructural crack paths between hypo-eutectic Al–Si–Cu and Al–Si–Mg cast alloys in high plasticity regimes under rotating bending, Materials Science and Engineering: A. 618 (2014) 578–585. https://doi.org/10.1016/j.msea.2014.08.062.
[16] L. Zeng, J. Sakamoto, A. Fujii, H. Noguchi, Role of eutectic silicon particles in fatigue crack initiation and propagation and fatigue strength characteristics of cast aluminum alloy A356, Engineering Fracture Mechanics. 115 (2014) 1–12. https://doi.org/10.1016/j.engfracmech.2013.11.016.
[17] D.D. Tian, X.S. Liu, G.Q. He, Y. Shen, S.Q. Lv, Q.G. Wang, Low cycle fatigue behavior of casting A319 alloy under two different aging conditions, Materials Science and Engineering: A. 654 (2016) 60–68.
[18] L. Wang, Influence of the casting microstructure on damage mechanisms in Al-Si alloys by using 2D and 3D in-situ analysis, PhD thesis, Ecole Centrale de Lille, 2015. https://tel.archives-ouvertes.fr/tel-01272159/document (accessed August 16, 2016).
[19] Gall, Yang, Horstemeyer, McDowell, Fan, The influence of modified intermetallics and Si particles on fatigue crack paths in a cast A356 Al alloy, Fat Frac Eng Mat Struct. 23 (2000) 159–172. https://doi.org/10.1046/j.1460-2695.2000.00239.x.
[20] J.Z. Yi, Y.X. Gao, P.D. Lee, T.C. Lindley, Effect of Fe-content on fatigue crack initiation and propagation in a cast aluminum-silicon alloy (A356-T6), Materials Science and Engineering A. 386 (2004) 396–407. https://doi.org/10.1016/j.msea.2004.07.044.
[21] L. Ceschini, I. Boromei, A. Morri, S. Seifeddine, I.L. Svensson, Microstructure, tensile and fatigue properties of the Al–10% Si–2% Cu alloy with different Fe and Mn content cast under controlled conditions, Journal of Materials Processing Technology. 209 (2009) 5669–5679.
[22] V. Firouzdor, M. Rajabi, E. Nejati, F. Khomamizadeh, Effect of microstructural constituents on the thermal fatigue life of A319 aluminum alloy, Materials Science and Engineering: A. 454–455 (2007) 528–535. https://doi.org/16/j.msea.2007.01.018.
[23] S. Dezecot, V. Maurel, J.-Y. Buffiere, F. Szmytka, A. Koster, 3D characterization and modeling of low cycle fatigue damage mechanisms at high temperature in a cast aluminum alloy, Acta Materialia. 123 (2017) 24–34.

[24] W.W. Bose-Filho, E.R. de Freitas, V.F. da Silva, M.T. Milan, D. Spinelli, Al–Si cast alloys under isothermal and thermomechanical fatigue conditions, International Journal of Fatigue. 29 (2007) 1846–1854. https://doi.org/10.1016/j.ijfatigue.2007.01.006.
[25] B. Guo, W. Zhang, S. Li, X. Wang, High temperature low cycle fatigue and creep-fatigue behavior of a casting Al-9Si-CuMg alloy used for cylinder heads, Materials Science and Engineering: A. 700 (2017) 397–405.
[26] S. Tabibian, E. Charkaluk, A. Constantinescu, F. Szmytka, A. Oudin, TMF–LCF life assessment of a Lost Foam Casting A319 aluminum alloy, International Journal of Fatigue. 53 (2013) 75–81. https://doi.org/10.1016/j.ijfatigue.2012.01.012.
[27] S. Tabibian, E. Charkaluk, A. Constantinescu, F. Szmytka, A. Oudin, TMF criteria for Lost Foam Casting aluminum alloys, Fatigue & Fracture of Engineering Materials & Structures. 36 (2013) 349–360. https://doi.org/10.1111/ffe.12006.
[28] G. Zhang, L. Bingchao, J. Zhang, W. Cai, The strain amplitude-controlled cyclic fatigue behavior of Al 2 O 3 fiber reinforced Al–Si alloy composite at elevated temperatures, Progress in Natural Science: Materials International. 22 (2012) 153–159.
[29] H. Arami, R. Khalifehzadeh, M. Akbari, F. Khomamizadeh, Microporosity control and thermal-fatigue resistance of A319 aluminum foundry alloy, Materials Science and Engineering: A. 472 (2008) 107–114. https://doi.org/16/j.msea.2007.03.031.
[30] M. Joyce, Elevated temperature short crack fatigue behaviour in near eutectic Al?Si alloys, International Journal of Fatigue. 25 (2003) 863–869. https://doi.org/10.1016/S0142-1123(03)00157-9.
[31] K. Gall, M. Horstemeyer, D.L. McDowell, J. Fan, Finite element analysis of the stress distributions near damaged Si particle clusters in cast Al-Si alloys, Mechanics of Materials. 32 (2000) 277–301. https://doi.org/10.1016/S0167-6636(00)00003-X.
[32] Y.X. Gao, J.Z. Yi, P.D. Lee, T.C. Lindley, A micro-cell model of the effect of microstructure and defects on fatigue resistance in cast aluminum alloys, Acta Materialia. 52 (2004) 5435–5449. https://doi.org/10.1016/j.actamat.2004.07.035.
[33] G. Lasko, M. Apel, A. Carré, U. Weber, S. Schmauder, Effect of Microstructure and Hydrogen Pores on the Mechanical Behavior of an Al7% Si0. 3% Mg Alloy Studied by a Combined Phase-Field and Micromechanical Approach, Advanced Engineering Materials. 14 (2012) 236–247.
[34] A. Saigal, E.R. Fuller, Analysis of stresses in aluminum-silicon alloys, Computational Materials Science. 21 (2001) 149–158. https://doi.org/10.1016/S0927-0256(00)00224-X.
[35] I. Bacaicoa, M. Wicke, M. Luetje, F. Zeismann, A. Brueckner-Foit, A. Geisert, M. Fehlbier, Characterization of casting defects in a Fe-rich Al-Si-Cu alloy by microtomography and finite element analysis, Engineering Fracture Mechanics. (2017). http://www.sciencedirect.com/science/article/pii/S0013794416305628.
[36] A. Brueckner-Foit, M. Luetje, I. Bacaicoa, A. Geisert, M. Fehlbier, On the role of internal defects in the fatigue damage process of a cast Al-Si-Cu alloy, Procedia Structural Integrity. 7 (2017) 36–43.
[37] O. Caty, J.Y. Buffiere, E. Maire, J. Adrien, 3D Characterization of the Influence of Porosity on Fatigue Properties of a Cast Al Alloy, Advanced Engineering Materials. 13 (2011) 194–198.
[38] S. Fintová, G. Anzelotti, R. Konečná, G. Nicoletto, Casting Pore Characterization by X-Ray Computed Tomography and Metallography, Archive of Mechanical Engineering. (2010) 263–273.
[39] P. Li, P.D. Lee, D.M. Maijer, T.C. Lindley, Quantification of the interaction within defect populations on fatigue behavior in an aluminum alloy, Acta Materialia. 57 (2009) 3539–3548. https://doi.org/10.1016/j.actamat.2009.04.008.
[40] M. Luetje, M. Wicke, I. Bacaicoa, A. Brueckner-Foit, A. Geisert, M. Fehlbier, 3D characterization of fatigue damage mechanisms in a cast aluminum alloy using X-ray tomography, International Journal of Fatigue. (2017).
[41] G. Nicoletto, R. Konečná, S. Fintova, Characterization of microshrinkage casting defects of Al–Si alloys by X-ray computed tomography and metallography, International Journal of Fatigue. 41 (2012) 39–46. https://doi.org/10.1016/j.ijfatigue.2012.01.006.
[42] I. Serrano-Munoz, J.-Y. Buffiere, C. Verdu, Casting defects in structural components: are they all dangerous? A 3D study, International Journal of Fatigue. (2018).
[43] K. Gall, M.F. Horstemeyer, B.W. Degner, D.L. McDowell, J. Fan, On the driving force for fatigue crack formation from inclusions and voids in a cast A356 aluminum alloy, International Journal of Fracture. 108 (2001) 207–233.

[44] M. Teranishi, O. Kuwazuru, S. Gennai, M. Kobayashi, H. Toda, Three-dimensional stress and strain around real shape Si particles in cast aluminum alloy under cyclic loading, Materials Science and Engineering: A. 678 (2016) 273–285.
[45] C.M. Dinnis, J.A. Taylor, A.K. Dahle, As-cast morphology of iron-intermetallics in Al-Si foundry alloys, Scripta Materialia. 53 (2005) 955–958. https://doi.org/10.1016/j.scriptamat.2005.06.028.
[46] F. Lasagni, A. Lasagni, M. Engstler, H.P. Degischer, F. Mücklich, Nano-characterization of Cast Structures by FIB-Tomography, Advanced Engineering Materials. 10 (2008) 62–66.
[47] J. Barrirero, M. Engstler, N. Ghafoor, N. de Jonge, M. Odén, F. Mücklich, Comparison of segregations formed in unmodified and Sr-modified Al–Si alloys studied by atom probe tomography and transmission electron microscopy, Journal of Alloys and Compounds. 611 (2014) 410–421. https://doi.org/10.1016/j.jallcom.2014.05.121.
[48] S. Dezecot, J.-Y. Buffiere, A. Koster, V. Maurel, F. Szmytka, E. Charkaluk, N. Dahdah, A. El Bartali, N. Limodin, J.-F. Witz, In situ 3D characterization of high temperature fatigue damage mechanisms in a cast aluminum alloy using synchrotron X-ray tomography, Scripta Materialia. 113 (2016) 254–258. https://doi.org/10.1016/j.scriptamat.2015.11.017.
[49] D. Paganin, S.C. Mayo, T.E. Gureyev, P.R. Miller, S.W. Wilkins, Simultaneous phase and amplitude extraction from a single defocused image of a homogeneous object, Journal of Microscopy. 206 (2002) 33–40. https://doi.org/10.1046/j.1365-2818.2002.01010.x.
[50] N. Dahdah, N. Limodin, A. El Bartali, J.F. Witz, R. Seghir, E. Charkaluk, J.Y. Buffiere, Damage Investigation in A319 Aluminium Alloy by X-ray Tomography and Digital Volume Correlation during In Situ High-Temperature Fatigue Tests, Strain. 52 (2016) 324–335. https://doi.org/10.1111/str.12193.
[51] V. Boulos, V. Fristot, D. Houzet, L. Salvo, P. Lhuissier, Investigating performance variations of an optimized GPU-ported granulometry algorithm, in: 2012 Conference on Design and Architectures for Signal and Image Processing (DASIP), 2012: pp. 1–6.
[52] Z. Li, A.M. Samuel, F.H. Samuel, C. Ravindran, S. Valtierra, Effect of alloying elements on the segregation and dissolution of CuAl2 phase in Al-Si-Cu 319 alloys, Journal of Materials Science. 38 (2003) 1203–1218. https://doi.org/10.1023/A:1022857703995.
[53] N. Dahdah, Influence des défauts de fonderie dans l'endommagement par fatigue thermomécanique oligocyclique d'un alliage d'aluminium obtenu par un procédé à modèle perdu, Thèse de doctorat, Ecole centrale de Lille, 2017. http://www.theses.fr/s153048 (accessed January 25, 2022).
[54] L. Wang, N. Limodin, A. El Bartali, J.-F. Witz, J.-Y. Buffiere, E. Charkaluk, Application of Synchrotron Radiation–Computed Tomography In-Situ Observations and Digital Volume Correlation to Study Low-Cycle Fatigue Damage Micromechanisms in Lost Foam Casting A319 Alloy, Metall Mater Trans A. 51 (2020) 3843–3857. https://doi.org/10.1007/s11661-020-05839-5.
[55] N. Limodin, A. El Bartali, L. Wang, J. Lachambre, J.-Y. Buffiere, E. Charkaluk, Application of X-ray microtomography to study the influence of the casting microstructure upon the tensile behaviour of an Al–Si alloy, Nuclear Instruments and Methods in Physics Research Section B: Beam Interactions with Materials and Atoms. 324 (2014) 57–62. https://doi.org/10.1016/j.nimb.2013.07.034.
[56] C.-L. Chen, Characterisation of intermetallic phases in multicomponent Al-Si alloys for piston applications, PhD thesis, Loughborough University, 2006.
[57] C.-L. Chen, A. Richter, R.C. Thomson, Investigation of mechanical properties of intermetallic phases in multi-component Al–Si alloys using hot-stage nanoindentation, Intermetallics. 18 (2010) 499–508. https://doi.org/10.1016/j.intermet.2009.09.013.
[58] C.J. Davidson, T.R. Finlayson, M.E. Fitzpatrick, J.R. Griffiths, E.C. Oliver, Q. Wang, Observations of the stress developed in Si inclusions following plastic flow in the matrix of an Al–Si–Mg alloy, Philosophical Magazine. 97 (2017) 1398–1417. https://doi.org/10.1080/14786435.2017.1296978.
[59] A. Pyzalla, A. Jacques, J.-P. Feiereisen, T. Buslaps, T. D'Almeida, K.-D. Liss, In-situ Analysis of the Microstrains During Tensile Deformation of an AlSi-MMC at Room Temperature and Elevated Temperature, Journal of Neutron Research. 9 (2001) 435–442. https://doi.org/10.1080/10238160108200175.
[60] S. Dézécot, Caractérisation et modélisation du rôle des défauts microstructuraux dans la fatigue oligocyclique des alliages d'aluminium de fonderie : Application au procédé à modèle perdu, These de doctorat, Lyon, 2016. http://www.theses.fr/2016LYSEI148 (accessed October 11, 2021).

[61] N. Limodin, Lien microstructure – mécanismes d'endommagement en fatigue : couplage de la tomographie à rayons X et des mesures de champs, Habilitation à Diriger des Recherches, Université de Lille, 2019. http://hdl.handle.net/20.500.12210/32301.
[62] M.G. Mueller, M. Fornabaio, G. Žagar, A. Mortensen, Microscopic strength of silicon particles in an aluminium–silicon alloy, Acta Materialia. 105 (2016) 165–175. https://doi.org/10.1016/j.actamat.2015.12.006.
[63] K. Gall, N. Yang, M. Horstemeyer, D.L. McDowell, J. Fan, The debonding and fracture of Si particles during the fatigue of a cast Al-Si alloy, Metall and Mat Trans A. 30 (1999) 3079–3088. https://doi.org/10.1007/s11661-999-0218-2.
[64] G. Requena, G. Garcés, M. Rodríguez, T. Pirling, P. Cloetens, 3D Architecture and Load Partition in Eutectic Al-Si Alloys, Advanced Engineering Materials. 11 (2009) 1007–1014.
[65] S. Tabibian, Contribution to thermomechanical fatigue criteria of Lost Foam Casting aluminium alloys, PhD thesis, Ecole Centrale de Lille, 2011.